ADVANCED MATERIALS
www.advmat.de

Enhanced Optical Transmission through MacEtch-Fabricated Buried Metal Gratings

*Runyu Liu, Xiang Zhao, Christopher Roberts, Lan Yu, Parsian K. Mohseni, Xiuling Li, Viktor Podolskiy, and Daniel Wasserman**

The integration of metallic components with optoelectronic devices is both essential (allowing electrical access) as well as of interest for a range of novel optical effects resulting from plasmonic, metamaterial, and subwavelength optical structures. A metal film providing a near-uniform lateral voltage (current) distribution represents an ideal electrical contact for a wide range of electro-optical devices. At the same time, the same free electrons that are responsible for the high DC conductivity of metals also dominate their optical properties. This can be observed in the wide and varied field of plasmonics, which is in large part geared toward leveraging the ability of metal/dielectric structures to confine light to subwavelength volumes, thus enhancing light–matter interaction, and potentially enabling next-generation nanophotonic devices. Unfortunately, the high conductivity and novel plasmonic effects associated with the free carriers in metals also cause metals to be highly reflective at optical frequencies and result in parasitic absorption of light via (ohmic) losses in plasmonic materials, limiting the functionality of many materials or devices with integrated metallic components, plasmonic, or otherwise.[1] Thus, the integration of metal into any optical or optoelectronic structure or device, while often providing very real benefits (subwavelength confinement, uniform electrical contact, etc.) is almost always accompanied by absorption and reflection losses compromising the ultimate performance of the optical structure or device.

Transmission of light through the smooth interface between two materials can be related to the change of material permittivity via the Fresnel equations. However, this simple relationship is violated in structured composites. All-dielectric "moth-eye" interfaces are known to reduce the reflectivity between two dielectric media by creating a surface layer with gradually changing refractive index.[2,3] Nanostructuring, or even simple "roughening," of semiconducting solar cell material can efficiently scatter incident radiation, increasing the path length for light in the detector structure and acting as an antireflection coating.[4–6] However, for the development of active devices, structuring the dielectric interface does little to enable efficient electrical contact, which requires the integration of (often highly reflective) conducting material with the devices' active dielectric components.

The optical response of reflecting structured metallic films can be modified by coupling the incident radiation to a special type of highly confined electromagnetic waves supported by thin metal films, surface plasmon polaritons (SPPs), followed by the out-coupling of SPPs into the dielectric on the other side of the film. Remarkably, the percentage of light transmitted through such structured metal films can exceed, at select frequencies, the percentage of open area in the films, a phenomenon known as extraordinary optical transmission (EOT), a source of substantial interest in the optics community since the initial demonstration of EOT nearly two decades ago.[7,8] More recent research, aimed at elucidation of the origin of EOT, has provided a number of complex coupled (and sometimes competing) mechanisms, related to the excitation, transmission, and out-coupling of (i) SPPs at the two metal–dielectric interfaces and (ii) waveguide modes supported by the openings in the perforated metal films.[9–13]

EOT structures have been touted as potential optical filters,[14] and they are also of significant interest as hybrid electrical contact/optical couplers for optoelectronic devices. A metal film capable of providing a near-uniform lateral voltage/current distribution over the surface of a device, yet also capable of controlling, and enhancing, the coupling of incident radiation into the device, has potential for a broad range of light-emitting and detecting optoelectronic devices. Such structures have been utilized for all-optical modulation of light–matter interaction,[15] active control of thin film transmission,[16–18] and to improve light absorption in underlying photodetector structures.[19–21] However, even without the losses from underlying active materials, passive EOT structures, from a purely light filtering standpoint, typically demonstrate un-normalized peak transmission efficiencies well below 50%, never approaching the performance of traditional multilayer thin film filters, especially at optical frequencies. The reason for this poor peak transmission is twofold, resulting from both weak coupling to the plasmonic structure from free space, as well as losses in the metal itself (more problematic at shorter wavelengths, where the excited surface modes are more tightly bound, and thus interact more

R. Liu, X. Zhao, L. Yu, Prof. X. Li, Prof. D. Wasserman
Department of Electrical and Computer Engineering
Micro and Nanotechnology Laboratory
University of Illinois
Urbana, IL 61801, USA
E-mail: dwass@illinois.edu
C. Roberts, Prof. V. Podolskiy
Department of Physics and Applied Physics
University of Massachusetts Lowell
One University Ave.
Lowell, MA 01854, USA
Prof. P. K. Mohseni
Microsystems Engineering
Rochester Institute of Technology
Rochester, NY 14623, USA

DOI: 10.1002/adma.201505111

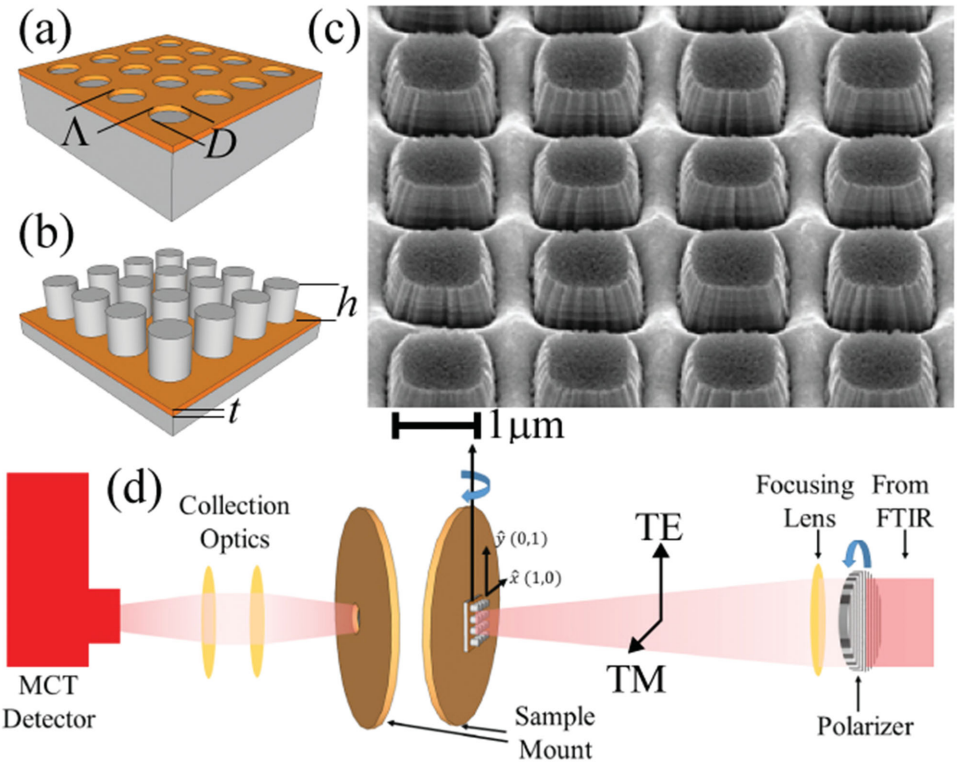

Figure 1. Schematic of an extraordinary transmission grating a) before and b) after the MacEtch process. c) 45° tilted view scanning electron microscope (SEM) image of a MacEtch-fabricated buried-EOT grating with $\Lambda = 1.75\,\mu m$, $D = 1.2\,\mu m$, and $h = 0.77\,\mu m$. Experimental setup for linearly polarized, angle-dependent transmission experiments.

strongly with the metal film).[22] It is worth noting that strong transmission (≈90%) through EOT arrays with apertures above cut-off, fabricated on glass, has been observed.[23] However, these structures demonstrate limited to no antireflection properties, as the low refractive index of glass already gives ≈96% transmission without the patterned metal layer.

In this work, we experimentally demonstrate an optical architecture which allows for the integration of a thin (≈10–30 nm) nanostructured metal (gold) film into a high-index semiconductor (GaAs) material and which can exhibit transmission exceeding that of a smooth air–semiconductor interface. We dub such structures "buried" EOT (B-EOT) gratings, and describe their fabrication using the metal-assisted chemical etching (MacEtch) process.[24,25] The resulting structures, which look similar to dielectric micro/nanopillars "extruded" through an EOT grating (**Figure 1**a,b), can be fabricated with subwavelength, nanoscale pitch, and feature size, with etch depths equal to or greater than the grating pitch. Our structures are modeled using 3D rigorous coupled wave analysis (RCWA) and characterized experimentally by angle-dependent Fourier transform infrared (FTIR) transmission spectroscopy with good agreement between the theoretical predictions and experimental results. We present the protocols for fabrication of such structures and comprehensive experimental and theoretical analysis of their optical response. B-EOT structures not only show significantly enhanced peak transmission when normalized to the open area of the metal film, but more importantly, peak transmission greater than that observed from the bare semiconductor surface. In a sense, the B-EOT structure combines the benefits of both moth-eye antireflection coatings and EOT-inspired spectral selectivity. The structures demonstrated are of particular interest for potential optoelectronic applications, especially for a range of integrated emitter and detector structures. Though we demonstrate passive structures in this work, the results presented offer the potential for efficient electrical and optical access to a range of active optoelectronic devices.

Normal incidence transmission spectra for B-EOT samples with pillar heights ranging from $h = 0$ to $1000\,nm$ are summarized in **Figure 2**. The fundamental phenomenon of interest is best seen in Figure 2a, where we show the RCWA simulated transmission for pillars of fixed lateral geometry and varying heights. Here, we only consider transmission at the top surface of the sample (ignoring the losses in the substrate and at the substrate/air interface on the bottom of the sample), which best demonstrates the antireflective nature of the B-EOT structures. The transmission spectra corresponding to $h = 0\,nm$ exhibit the Fano-type response characteristic of EOT gratings.[7,26–28] The spectral positions of the (1,0) and (1,1) EOT resonances at $\lambda_{1,0} = 5.76\,\mu m$ and $\lambda_{1,1} = 4.07\,\mu m$ (Figure 2a) correspond to coupling of light into propagating SPPs at the GaAs–metal interface through the lowest diffraction orders of the grating formed by the B-EOT structure. As the pillar height h is increased (as the EOT grating is buried deeper into the substrate), the transmission spectrum changes dramatically, with a marked increase in the transmission peak's long-wavelength

Adv. Mater. **2015**,
DOI: 10.1002/adma.201505111

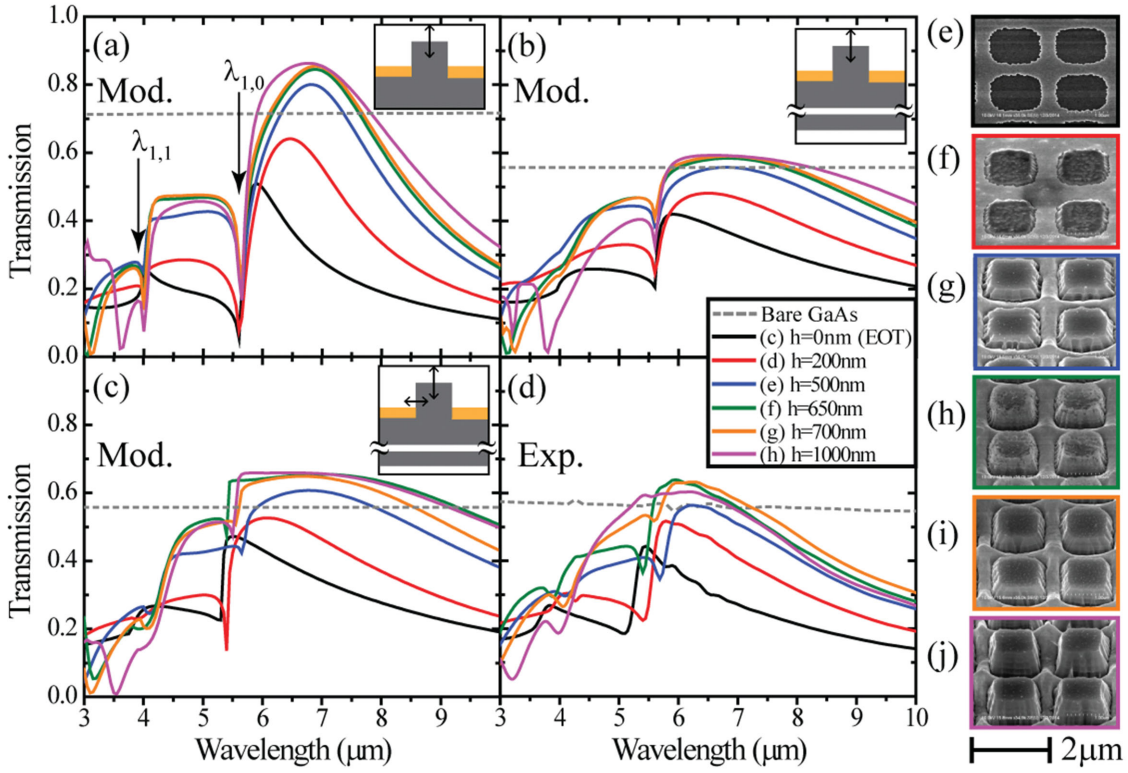

Figure 2. 3D RCWA simulations of transmission for varying pillar heights for a) top surface transmission, assuming fixed lateral geometry ($\Lambda = 1.75\,\mu m$ and diameter $D = 1.2\,\mu m$), b) transmission through top and bottom interfaces, assuming the same fixed lateral geometry, and c) transmission through top and bottom interfaces, with varying lateral geometries measured on fabricated samples using SEM. d) Experimental normal incidence transmission spectra for B-EOT structures with designed $\Lambda = 1.75\,\mu m$ and diameter $D = 1.2\,\mu m$, for varying etch depths (h). The unetched sample ($h = 0$ nm), corresponding to a traditional EOT grating, is shown in black. Transmission through an unpatterned SI GaAs wafer is also shown for comparison (dashed gray). Scanning electron images of individual pillars from the samples with spectra shown in (d), having etch depths of e) $h = 0$ nm, f) $h = 200$ nm, g) $h = 500$ nm, h) $h = 650$ nm, i) $h = 700$ nm, and j) $h = 1000$ nm. All SEM images are taken at a 45° tilt.

tail. This effect is most clearly seen in Figure 2a, with predicted peak transmission reaching ≈90% at $\lambda \approx 7\,\mu m$, an increase in transmission of almost 20% when compared to the bare, smooth GaAs–air surface. The experimental data show similar qualitative results, with a narrow transmission peak of ≈40% for the unetched EOT sample and a broader transmission peak, reaching ≈65% for the $h = 650$ nm and $h = 700$ nm samples. As in the numerical solutions of Maxwell's equations, the peak experimental transmission through the B-EOT sample is larger than the transmission through the bare GaAs wafer at the same wavelength.

However, comparing our simulations of Figure 2a to the experimental data of Figure 2d, we see that while the qualitative behavior of the grating is replicated in the RCWA simulations, minor adjustments are required to achieve a realistic simulation of our experimental parameters. First, in Figure 2b, we consider the effect of the substrate on the transmission, by modeling the substrate as a thick, incoherent layer (where the RCWA code ignores the phase information of light transmitted into the substrate). We see that when the substrate effects are considered, the overall transmission of our simulations shows good agreement with our experimental results, most easily observed in the bare GaAs simulations, which shows a drop in transmission from ≈70% to ≈57%. More subtly, we also observe spectral shifts between the experimental data and the simulated transmission of Figure 2 a,b. The likely reason for this shift comes from the evolution of the sample geometry throughout the MacEtch process. Most notably, a shift in the periodicity of the metal mesh is observed (from $\Lambda = 1.65\,\mu m$ to $\Lambda = 1.75\,\mu m$) between the unetched EOT sample and all of the MacEtched samples. This effect is a result of a resizing of the Au mesh upon initiation of the MacEtch process and has been observed in previous MacEtch work.[29,30] For this reason, we also used measurements of the lateral geometry of our samples (from scanning electron microscope (SEM) measurements) to simulate the exact structure geometries (as well as the substrate effects) for each of the etch depths characterized experimentally. These simulations are shown in Figure 2c, and show good spectral agreement with our experimental data.

Finally, the distinct spectral features observed in the simulated transmission spectra resulting from SPP coupling (i.e., the strong dip at $\lambda \approx 5.5\,\mu m$) are somewhat weaker in the experimental data for the deeper-etched samples, an effect possibly resulting from the nonuniformity in individual pillar width, and between pillar heights, associated with longer etch times. While we are able to achieve good agreement between our experimental and simulated transmission spectra, it is important to note that the observed spectral response is

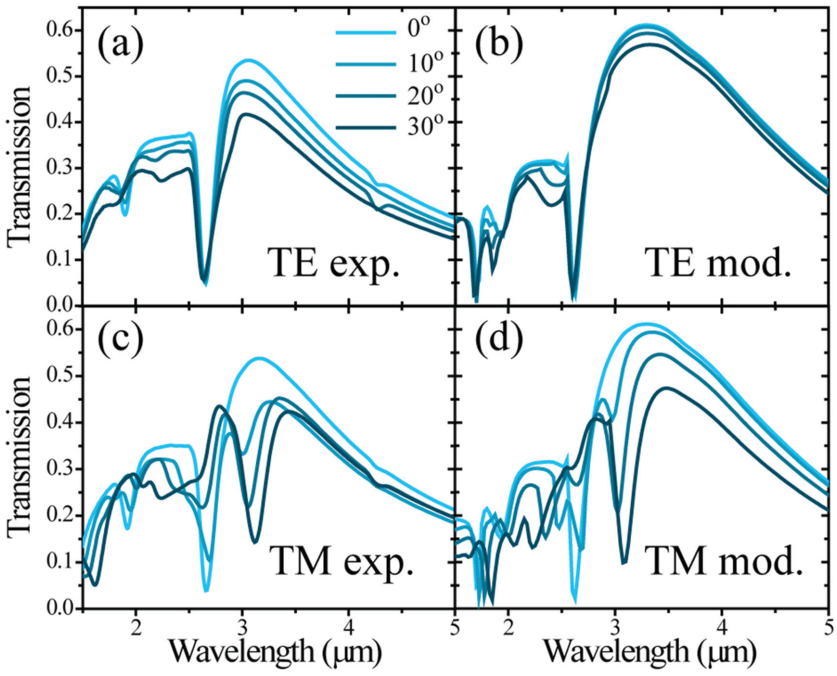

Figure 3. Comparison of a,b) TE and c,d) TM transmission as a function of the incident angle for angles from $\theta = 0^\circ$ to $\theta = 30$. The sample under test has period $\Lambda = 0.77\,\mu m$, diameter $D = 0.55\,\mu m$, and pillar height $h = 500$ nm. a,c) Experimental results and b,d) simulation results (including substrate effects). The small minima at $\lambda \approx 4.3\,\mu m$ observed in some of the spectra in (a) and (b) results from small changes in CO_2 absorption between background and sample spectra.

dominated by the front structured interface, as best depicted in the calculations that ignore substrate effects (Figure 2a), while the back interface of the system provides the overall spectrally flat correction to the results. Regardless of the back interface, our results demonstrate that the B-EOT structure, despite covering ≈50% of the sample surface with metal, acts as an antireflection coating over a reasonably broad range of the mid-infrared.

Angular-dependent transmission data for two different samples ($\Lambda = 0.77\,\mu m$, $D = 0.55\,\mu m$, and $h = 0.5\,\mu m$, and $\Lambda = 1.75\,\mu m$, $D = 1.2\,\mu m$, and $h = 0.7\,\mu m$) are shown in **Figures 3** and **4** for both TE and TM polarized light, respectively. As can be seen in Figures 3a and 4a, the TE-polarized transmission peaks for each sample remain reasonably large and (spectrally) stationary for incidence angles up to 30°, with the dips in the spectrum [associated with (0,1) SPP coupling] remaining fixed in position and magnitude (as would be expected for incident light with unchanging momentum in the direction of SPP propagation). Splitting in the (1,1) SPP-coupling feature is observed for the TE spectra, as non-normal incident TE-polarized light will have a varying momentum component in the (1,1) directions with increasing incidence angle.

The TM polarized data (Figures 3c and 4c) differ from the TE data in two significant regards. First, as the sample is rotated away from normal, we see a weakening in the transmission dips associated with SPP-coupling, as would be expected for incident light with momentum components in the direction of SPP propagation, which will lift the wavelength degeneracy of the positive and negative propagating (1,0) and (1,1) SPPs excited at the Au/GaAs interface. Interestingly, we see the appearance of a strong dip in the center of each samples' primary transmission peak, which grows in magnitude as the incidence angle increases. RCWA simulations for each sample for both TE-polarized (Figures 3b and 4b) and TM-polarized (Figures 3d and 4d) incident radiation, including substrate effects, show good agreement with experimental data.

The results from our 3D RCWA simulations of the fabricated B-EOT structures offer insight into both the primary finding of this work (namely, the strongly enhanced transmission seen with increasing pillar height) and the spectral anomalies observed in our angular-dependent transmission (strong dips in TM-polarized transmission with increasing angle). Our models suggest that the high reflectivity of the planar GaAs–air and metal–air interfaces is modulated through coupling of light into waveguide-type modes supported by the pillar arrays. Figure 4e shows the local Poynting flux (color scale) and Poynting vector field lines for normal incidence light at $\lambda_o = 7.1\,\mu m$, indicating strong transmission is associated with coupling into the dielectric pillar. Figure 4f illustrates the coupling of incident energy to the thin metal film (note the Poynting vector field lines ending at the metal), giving the transmission dip at oblique (30°) incidence at the same wavelength. Both Figure 4e,f are modeled without effects related to incoherent back interface of the structure, as the purpose of these calculations is to elucidate the behavior of our structures only in the near field of the B-EOT gratings.

Unlike a traditional EOT grating, where peak transmission can be thought of as an interference maximum associated with light directly transmitted through the arrayed apertures and light scattered from surface modes, the transmission peak in our B-EOT samples results from efficient avoidance of coupling to plasmonic modes. Indeed, transmission through a pillar structure with no metal film shows broadband antireflection properties (**Figure 5**). Note that the simulations in Figure 5 ignore absorption/reflection in the substrate, so as to elucidate the optical properties of the top patterned surface that dominates the spectral response of the structure. Such coupling cannot be avoided for all wavelength/angle/polarization combinations. As a result, the narrow-band angle-dependent transmission minima appear at higher angles along with the broader antireflection (enhanced transmission) background. These minima are associated with the coupling into, and absorption by, the thin metal film, as evidenced by the inset in Figure 4f showing the local Poynting flux and vector field lines for 30° incidence angle light at $\lambda_o = 7.1\,\mu m$. The spectral position of this minimum depends on the geometrical parameters of B-EOT structures. In our simulations, we modeled the nanopillar cross section as a Lamé curve, $|x|^N + |y|^N \le R^N$ keeping the ratio of pillar "diameter" to the unit cell size constant. When

Adv. Mater. **2015**,
DOI: 10.1002/adma.201505111

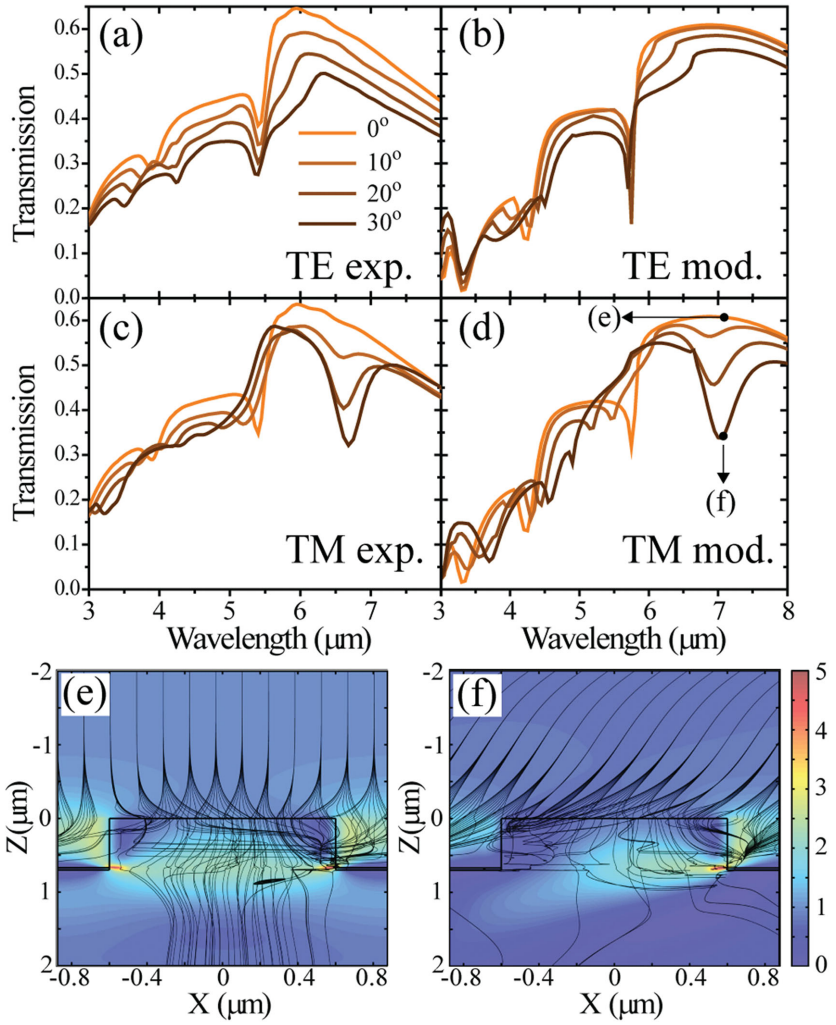

Figure 4. Comparison of TE and TM transmission as a function of incident angle for angles from $\theta = 0^\circ$ to $\theta = 30^\circ$. The sample under test has period $\Lambda = 1.75\,\mu m$, diameter $D = 1.2\,\mu m$, and pillar height $h = 700\,nm$. a,c) Experimental results, b,d) simulation results (including substrate effects) for a,b) TE- and c,d) TM-polarized incident light. Contour plots of calculated local Poynting flux (not including substrate effects) for e) $\theta = 0^\circ$ and f) $\theta = 30^\circ$ at $\lambda = 7.1\,\mu m$, with lines showing Poynting vector field lines.

the pillars have circular cross sections ($N = 2$) the spectral position of metal-transmission minimum is well described by diffraction theory (Figure 5b)

$$\lambda_{m,n}(\theta_i) = \frac{\Lambda}{\sqrt{m^2+n^2}}\left(\sqrt{\frac{\varepsilon_{Au}\varepsilon_{GaAs}}{\varepsilon_{Au}+\varepsilon_{GaAs}}} \mp \sin(\theta_i)\right)$$
$$\simeq \frac{\Lambda}{\sqrt{m^2+n^2}}\left(n_{GaAs} \mp \sin(\theta_i)\right) \quad (1)$$

where m,n give the order of the diffracted mode in 2D and θ_i is the angle of incidence, from normal. As the shape of the pillar becomes more square-like ($N > 2$), and as a larger percentage of the unit cell is occupied by the dielectric, the position of the broad metal-related minimum red-shifts and becomes less dependent on the incident angle (Figure 5f). Note that this spectrally stationary absorption maximum splits off the weak (but spectrally sharp) absorption peak that is still described by Equation (1). Reproducing the sharp, square features of our lithography mask in our metal film becomes more difficult with decreasing feature size, an effect that turns squares into quasi-circles with decreasing Λ. Thus, our $\Lambda = 1.75\,\mu m$ samples have almost square openings, approximated here as Lamé curves with $N \simeq 6$, while the $\Lambda = 0.77\,\mu m$ samples have almost-circular openings ($N \simeq 2$). As expected, our larger period samples show TM-polarized transmission dips which remain nearly spectrally stationary with increasing angle (Figure 4c) while the same dip, in our smaller period sample shows a continuous red shift with increasing angle (Figure 3c).

Figure 6 shows the calculated transmission, at normal incidence, for fixed wavelength $\lambda_o = 7.1\,\mu m$, as a function of pillar height. It is clearly seen that transmission oscillates with typical period $\Delta h \approx 1.9\,\mu m$. Analysis of propagating modes supported by a layer of periodic dielectric pillars suggests that the transmission of light through this layer is dominated by modes with propagation constant $k_z^m \simeq 1.6\,\mu m^{-1}$; note that $\Delta h \simeq \pi / k_z^m$. This fact further confirms that the observed transmission of light through the structured composite is in fact related to in-coupling of incident radiation into these modes. The insets of Figure 6 illustrate the behavior of light in the above mode, showing the z-component of Poynting flux (color scale) and the distribution of magnetic field across the unit cell. Note that the latter is extremely similar to the field profile of the plane wave, explaining the relatively easy coupling of light incident from free-space into the pillar array. On the other hand, the majority of energy flux is funneled into the dielectric pillar, thus assisting the transfer of this energy through the metal mesh at the interface between the pillar array and the homogeneous GaAs substrate.

The MacEtch process was used to fabricate buried extraordinary optical transmission gratings, metallic films with periodic arrays of subwavelength apertures buried into a high-index semiconductor material. The fabricated structures offer not only the uniform electrical contact expected from continuous metallic thin films, but perhaps more importantly, the potential for a significant enhancement of optical transmission, when compared to a bare, high-index semiconductor A. B-EOT structures are fabricated and experimentally characterized using FTIR transmission spectroscopy, demonstrating transmission as large as 65% (uncorrected for substrate losses and scattering) from a structure where a metal film covers ≈50% of the sample surface. We model the fabricated structures using 3D RCWA with good agreement to our experimental data. In addition, our model allows for a fundamental understanding

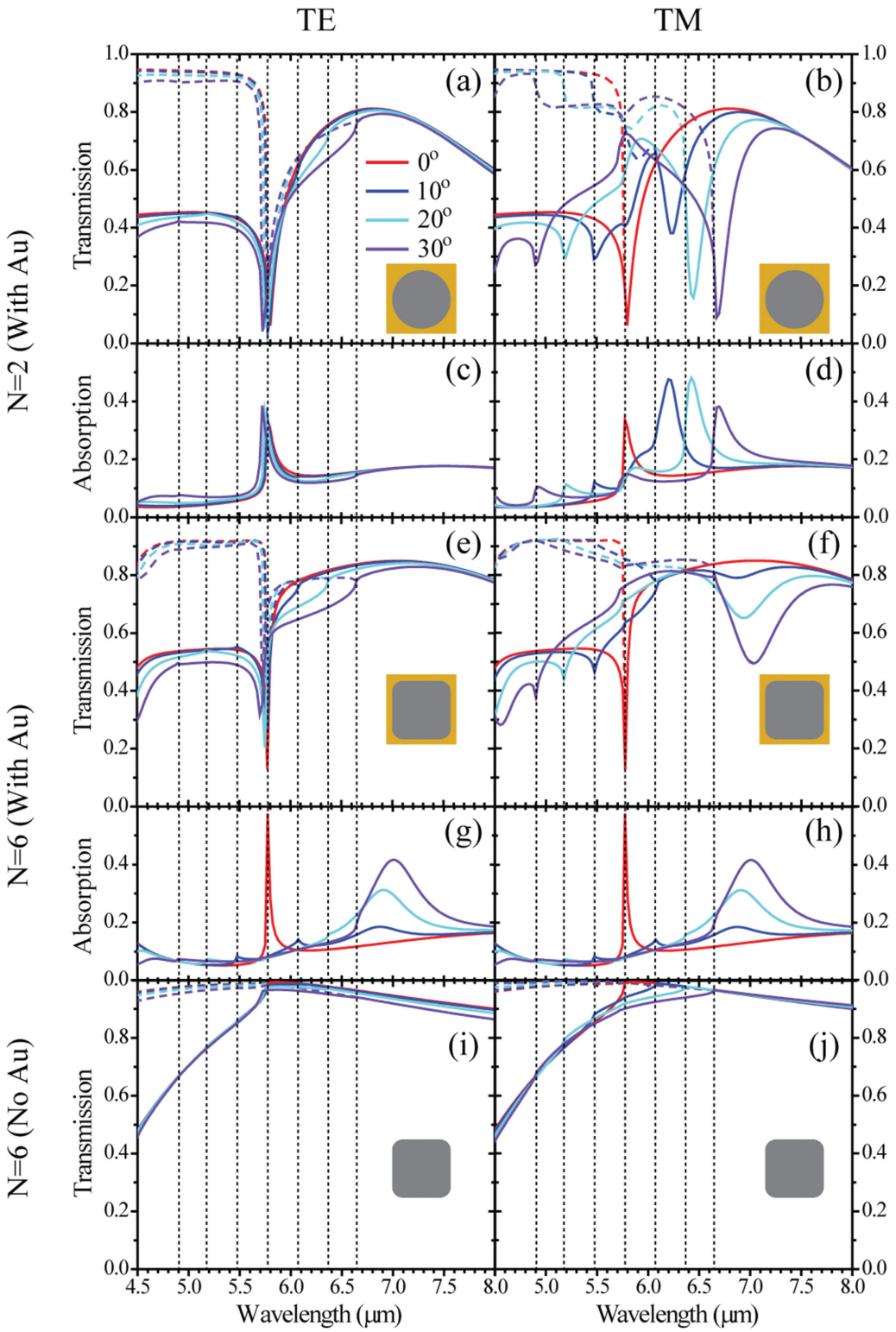

Figure 5. Comparison of a,b,e,f,i,j) numerically calculated TE and TM specular and total transmission and c,d,g,h) total absorption for B-EOT samples as a function of incident angle and pillar cross section for angles from $\theta = 0^{\circ}$ to $\theta = 30^{\circ}$. The specular transmission (solid lines) corresponds to the transmission collected experimentally, while the total (dashed lines) also includes light coupled into transmitted diffracted orders. The sample has period $\Lambda = 1.75\,\mu m$, diameter $D = 1.2\,\mu m$, and pillar height $h = 700\,nm$. a–d) A perfect circular pillar ($N = 2$), e–h) simulations for an $N = 6$ Lamé curve pillar cross section, and i,j) an $N = 6$ Lamé curve pillar cross section with no Au grating. The dotted vertical lines correspond to the spectral positions of the first order SPP coupling. No absorption is shown for the sample without Au, as the GaAs is modeled as a lossless dielectric. Insets in transmission plots show modeled pillar cross section.

Adv. Mater. **2015**,
DOI: 10.1002/adma.201505111

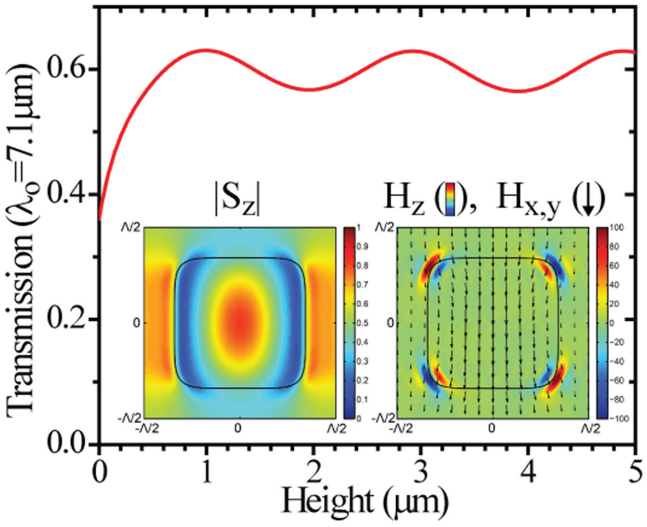

Figure 6. Numerically calculated peak transmission ($\lambda_o = 7.1\,\mu m$) through B-EOT structure (period $\Lambda = 1.75\,\mu m$, diameter $D = 1.2\,\mu m$) as a function of pillar height (h) (including substrate effects). Insets show cross-sectional field profile inside the pillar for (left) the z-component of the Poynting vector and (right) the in-plane (arrows) and z- (color) components of the magnetic field.

of the dielectric pillar-mediated transmission enhancement, as well as additional spectral features observed in the angle-dependent transmission experiments. Typically, the integration of metallic structures with semiconductor materials and/or optoelectronic devices requires a trade-off between efficient electrical contact (metal coverage) and optical coupling to free space (open, metal-free surface). The structures presented here, however, realize efficient, low-loss integration of metallic films with high-index semiconductor materials, offering the opportunity for next-generation optoelectronic sources and detectors with efficient electrical and optical access.

Experimental Section

Sample Fabrication: The B-EOT structures characterized in this work were fabricated by MacEtch of double-side polished semi-insulating (SI) GaAs (100) substrates. MacEtch is a wet but directional semiconductor (e.g., Si, SiGe, GaAs, InP, GaN, etc.) etching technique which involves a thin layer of noble metal (e.g., Au, Pt, etc.) acting as a catalyst to guide the etch process in a solution that usually consists of an oxidant (to generate holes) and an acid (to remove the oxidized species).[31–33] Under controlled etch conditions, only the semiconductor material directly underneath the catalyst metal is removed. This results in the catalyst metal being "engraved" or "buried" into the semiconductor, leaving behind a 3D semiconductor pattern that is complementary to the metal pattern. The sidewall roughness of MacEtch-produced semiconductor structures is largely determined by the catalyst metal pattern edge roughness. The sidewall verticality is affected by competing etching processes when mass transport of the oxidized species is limited. Details of the MacEtch mechanism, characteristics, and applications can be found elsewhere.[24,25,34–36] In this work, all samples were initially cleaned with a diluted HCl solution to remove the native oxide in order to ensure an intimate contact between the deposited Au film and the underlying GaAs, critical to the uniformity and effectiveness of the MacEtch process. Following the oxide etch, a 30 nm thick Au film was deposited across the entire sample surface by e-beam evaporation, after which a layer of SU-8 (thickness ≈5 μm) is spun over the Au. Polydimethylsiloxane (PDMS) stamps, consisting of a 2D array of holes with periodicities $\Lambda = 0.77\,\mu m$ and $\Lambda = 1.75\,\mu m$, were used to pattern the Au film by soft lithography. The periodic patterns on the PDMS stamps were transferred to the SU-8 coated samples by manually pressing the stamps against the samples, followed by a cure at 95 °C, leaving an SU-8 film with a 2D periodic array of apertures. After etching of the exposed Au film using TFAC Au etchant through the SU-8 etch mask, the SU-8 was stripped from the sample leaving an Au film with a periodic hole array on the GaAs substrate. The MacEtch process was then performed using a solution containing $KMnO_4$ (0.025 g) and HF (15 mL) diluted by de-ionized water (15 mL),[29,30] etching only the material under the patterned Au film at an etch rate of $\approx 118 \pm 10$ nm min^{-1} as measured by SEM. Controlling etch time effectively allows the Au to "descend" through the underlying semiconductor substrate, leaving the "extruded" GaAs pillars extending through the apertures in the Au film, as shown in Figure 1c. The resulting diameter and period of the GaAs pillars are controlled by the geometry of the patterned Au hole array, now "buried" at the base of the GaAs pillars following the MacEtch process, with the height of the GaAs pillars determined by the duration of the MacEtch.

Measurements: The transmission properties of the fabricated samples were characterized using a Bruker Vertex70 FTIR spectrometer in an experimental setup shown schematically in Figure 1d. Collimated light from the FTIR's broadband internal glo-bar was focused using an 8 in. focal length, 2 in. diameter ZnSe lens onto the sample, held outside the FTIR on a brass mount with a 2 mm diameter aperture, and with the aperture array's principle axes in the horizontal (1,0) and vertical (0,1) directions, as shown in Figure 1d. Light transmitted through the sample was collimated and refocused onto a liquid nitrogen-cooled HgCdTe (MCT) detector using a pair of 2 in. diameter, 3 in. focal length ZnSe lenses. The sample itself is mounted on a rotational stage with a principle axis of the 2D array aligned to the rotational axis of the stage to enable angular-dependent transmission measurements. A holographic wire grid polarizer was inserted between the first focusing lens and the sample, allowing for horizontally or vertically polarized incident radiation, corresponding to TM or TE polarization, respectively. Transmission spectra as a function of angle were taken for angles from 0° to 30° for both TM and TE polarized light. All transmission spectra are normalized to transmission through the experimental system with no sample on the mounting plate, providing an absolute transmission spectra for the fabricated samples. Transmission spectra through an unpatterned SI GaAs wafer were also collected, and are shown for comparison.

Modeling and Simulation: The fabricated structures were modeled using a 3D RCWA approach. This technique, originally introduced in ref. [37] and further expanded in ref. [38], takes explicit advantage of the periodicity of the B-EOT structure, imposing a Bloch-wave-periodicity condition on the fields. Explicitly, each planar region of the multilayer system (air, GaAs pillars in air, GaAs pillars in metal, homogeneous GaAs) is considered separately. For the simulations presented in this work, the following material parameters are used: $\varepsilon_{GaAs} = 10.89$ and $\varepsilon_{Au} = \varepsilon_B - \frac{\omega_p^2}{\omega^2 + i\omega\Gamma}$, with $\varepsilon_B = 9.5$, $\omega_p = 1.3597 \times 10^{16}$ Hz, and $\Gamma = 1.0486 \times 10^{14}$ Hz.

The electromagnetic field inside each region is represented as

$$\left[\vec{E},\vec{H} \propto \vec{E},\vec{H}(x,y)\exp\left(i\vec{q}\cdot\vec{\Lambda} + ik_z z\right)\right] \quad (2)$$

where $\hat{z}$ corresponds to the direction normal to the layered system. Substitution of Equation (2) into Maxwell's equations yields an eigenvalue-like problem. Each solution to this problem describes an individual electromagnetic mode, with an eigenvalue representing the mode's propagation constant k_z, which describes the evolution of the field along the $\hat{z}$ direction, and the eigenvector representing the field distribution across the unit cell. The electromagnetic field inside the system is then represented as a linear combination of the modes. At the final stage of the RCWA process, the amplitudes of the modes in each layer are related to the amplitudes of the modes in the neighboring

layers; implementation of RCWA[39] enforces the continuity of the tangential components of the E,H fields to calculate modal amplitudes.

The 3D RCWA technique was used to analyze the transmission, reflection, and absorption of the B-EOT structures described in the main text. The normal vector method was used to improve the convergence of in-plane components of the electric and displacement fields in the RCWA formalism.[40] The electromagnetic fields are represented as a finite Fourier series of the fields' modal amplitudes

$$\vec{E},\vec{H}(x,y,z)=\sum_{n=-N}^{N}\sum_{m=-M}^{M}(\vec{E},\vec{H})_{nm}\exp\left(i\vec{k}_{nm}\,\vec{r}\right) \quad (3)$$

where n,m are the Bloch indices of the modes. The Fourier representation suffers from Gibbs' phenomena at discontinuities in the permittivity. Lanczos' σ-factors were introduced to attenuate Gibbs phenomena in the reconstruction of the fields and improve the convergence of the Fourier series. The addition of the Lanczos' σ-factors alters the field reconstruction

$$\vec{E},\vec{H}(x,y,z)=\sum_{n=-N+1}^{N-1}\sum_{m=-M+1}^{M-1}\sigma_{nm}\left(\vec{E},\vec{H}\right)_{nm}\times\exp\left(i\vec{k}_{nm}\,\vec{r}\right) \quad (4)$$

where $\sigma_{nm}=\mathrm{sinc}(\pi n/N)\mathrm{sinc}(\pi m/M)$.[41,42]

To analyze the effects of the back interface of the structure, RCWA was used to calculate the transmission and reflection of the top structured interface for light incident from air and from the semiconductor. These calculations yield a matrix, $\hat{T}_{tt}$ that relates the intensity of the beam(s) incident from air onto the structured surface to intensities of the beams transmitted into the substrate. The calculations also yield a matrix $\hat{R}_{tb}$ that relates the intensities of the beams that approach the interface from within the semiconductor to the intensities of the beams reflected back into semiconductor. In a separate calculation, intensity-based transmission and reflection of the back interface was calculated for each diffracted beam that can be produced by the structured interface. These calculations yield (diagonal) matrices $\hat{T}_{bt}$ and $\hat{R}_{bt}$. Finally, total transmission through the structure was calculated as $\hat{T}_{tot}=\hat{T}_{bt}\left[\hat{I}+\hat{R}_{tb}\hat{R}_{bt}+\left(\hat{R}_{tb}\hat{R}_{bt}\right)^2+\left(\hat{R}_{tb}\hat{R}_{bt}\right)^3+\ldots\right]\hat{T}_{tt}$. This procedure is identical to averaging the optical response of the system over multiple thicknesses of the substrate, which physically represents the loss of coherence across the substrate layer.

Acknowledgements

R.L., X.Z., and C.R. contributed equally to this work. D.W. and R.L. acknowledge support from National Science Foundation grant DMR-1210398. V.P. and C.R. acknowledge support from National Science Foundation grant DMR-1209761. X.L. and X.Z. acknowledge support National Science Foundation grant CMMI 14-62946 and a gift from Lam Research Corporation.

Received: October 16, 2015
Published online:

[1] J. B. Khurgin, A. Boltasseva, *MRS Bull.* **2012**, *37*, 768.
[2] P. B. Clapham, M. C. Hurtley, *Nature* **1973**, *244*, 281.
[3] S. J. Wilson, M. C. Hurtley, *Opt. Acta* **1982**, *29*, 993.
[4] E. Yablonovitch, G. D. Cody, *IEEE Trans. Electron Devices* **1982**, *29*, 300.
[5] L. Zeng, Y. Yi, C. Hong, J. Liu, N. Feng, X. Duan, L. C. Kimerling, B. A. Alamariu, *Appl. Phys. Lett.* **2006**, *89*, 111111.
[6] Y. F. Huang, S. Chattopadhyay, Y.-J. Jen, C.-Y. Peng, T.-A. Liu, Y.-K. Hsu, C.-L. Pan, H.-C. Lo, C.-H. Hsu, Y.-H. Chang, C.-S. Lee, K.-H. Chen, L.-C. Chen, *Nat. Nanotechnol.* **2007**, *2*, 770.
[7] T. W. Ebbesen, H. J. Lezec, H. F. Ghaemi, T. Thio, P. A. Wolff, *Nature* **1998**, *391*, 667.
[8] H. Ghaemi, T. Thio, D. Grupp, T. W. Ebbesen, H. Lezec, *Phys. Rev. B* **1998**, *58*, 6779.
[9] M. Sarrazin, J.-P. Vigneron, J.-M. Vigoureux, *Phys. Rev. B* **2003**, *67*, 085415.
[10] J. Bravo-Abad, A. Degiron, F. Przybilla, C. Genet, F. J. García-Vidal, L. Martín-Moreno, T. W. Ebbesen, *Nat. Phys.* **2006**, *2*, 120.
[11] K. G. Lee, Q.-H. Park, *Phys. Rev. Lett.* **2005**, *95*, 103902.
[12] D. Pacifici, H. Lezec, H. A. Atwater, J. Weiner, *Phys. Rev. B* **2008**, *77*, 115411.
[13] H. Liu, P. Lalanne, *Nature* **2008**, *452*, 728.
[14] C. Genet, T. W. Ebbesen, *Nature* **2007**, *445*, 39.
[15] D. Pacifici, H. J. Lezec, H. A. Atwater, *Nat. Photonics* **2007**, *1*, 402.
[16] T. Ribaudo, E. A. Shaner, S. S. Howard, C. Gmachl, X. J. Wang, F.-S. Choa, D. Wasserman, *Opt. Express* **2009**, *17*, 7019.
[17] J. G. Rivas, P. H. Bolivar, H. Kurz, *Opt. Lett.* **2004**, *29*, 1680.
[18] K. Anglin, T. Ribaudo, D. C. Adams, X. Qian, W. D. Goodhue, S. Dooley, E. A. Shaner, D. Wasserman, *J. Appl. Phys.* **2011**, *109*, 123103.
[19] W. Wu, A. Bonakdar, H. Mohseni, *Appl. Phys. Lett.* **2010**, *96*, 161107.
[20] S. C. Lee, S. Krishna, S. R. J. Brueck, *Opt. Express* **2009**, *17*, 23160.
[21] R. Liu, P. Vasinajindakaw, G. Gu, J. Vaillancourt, X. Lu, *J. Phys. D: Appl. Phys.* **2013**, *46*, 015102.
[22] S. Law, V. Podolskiy, D. Wasserman, *Nanophotonics* **2013**, *2*, 103.
[23] K. L. van der Molen, F. B. Segerink, N. F. van Hulst, L. Kuipers, *Appl. Phys. Lett.* **2004**, *85*, 4316.
[24] X. Li, P. W. Bohn, *Appl. Phys. Lett.* **2000**, *77*, 2572.
[25] X. Li, *Curr. Opin. Solid State Mater. Sci.* **2011**, *16*, 71.
[26] C. Genet, M. P. Van Exter, J. P. Woerdman, *Opt. Commun.* **2003**, *225*, 331.
[27] S. Collin, G. Vincent, R. Haïdar, N. Bardou, S. Rommeluère, J.-L. Pelouard, *Phys. Rev. Lett.* **2010**, *104*, 027401.
[28] J. W. Yoon, J. H. Lee, S. H. Song, R. Magnusson, *Sci. Rep.* **2014**, *4*, 5683.
[29] M. DeJarld, J. C. Shin, W. Chern, D. Chanda, K. Balasundaram, J. A. Rogers, X. Li, *Nano Lett.* **2011**, *11*, 5259.
[30] P. K. Mohseni, S. H. Kim, X. Zhao, K. Balasundaram, J. D. Kim, L. Pan, J. A. Rogers, J. J. Coleman, X. Li, *J. Appl. Phys.* **2013**, *114*, 064909.
[31] Y. Yasukawa, H. Asoh, S. Ono, *Electrochem. Commun.* **2008**, *10*, 757.
[32] Y. Yasukawa, H. Asoh, S. Ono, *Jpn. J. Appl. Phys.* **2010**, *49*, 116502.
[33] S. H. Kim, P. K. Mohseni, Y. Song, T. Ishihara, X. Li, *Nano Lett.* **2014**, *15*, 641.
[34] K. Balasundaram, P. K. Mohseni, Y.-C. Shuai, D. Zhao, W. Zhou, X. Li, *Appl. Phys. Lett.* **2013**, *103*, 214103.
[35] Z. Huang, N. Geyer, P. Werner, J. De Boor, U. Gösele, *Adv. Mater.* **2011**, *23*, 285.
[36] Y. Yasukawa, H. Asoh, S. Ono, *J. Electrochem. Soc.* **2012**, *159*, 328.
[37] M. G. Moharam, T. K. Gaylord, *J. Opt. Soc. Am.* **1981**, *71*, 811.
[38] M. G. Moharam, E. B. Grann, D. A. Pommet, T. K. Gaylord, *J. Opt. Soc. Am. A* **1995**, *12*, 1068.
[39] C. Roberts, V. Podolskiy, Repository for RCWA code, http://viktor-podolskiy-research.wiki.uml.edu/RCWA (accessed: August 2015).
[40] T. Schuster, J. Ruoff, N. Kerwin, S. Rafler, W. Osten, *J. Opt. Soc. Am. A* **2007**, *24*, 2880.
[41] C. Lanzcos, *Applied Analysis, Dover Books on Mathematics*, Courier Corporation, NY **1988**, p. 225.
[42] R. W. Hamming, *Numerical Methods for Science and Engineers, Dover Books on Mathematics*, Courier Corporation, NY, USA **2012**, p. 527.